

Spider Silk Protein Forms Amyloid-Like Nanofibrils through a Non-Nucleation-Dependent Polymerization Mechanism

Xingmei Qi, Yu Wang, Hairui Yu, Ruifang Liu, Axel Leppert, Zihan Zheng, Xueying Zhong, Zhen Jin, Han Wang, Xiaoli Li, Xiuzhe Wang, Michael Landreh, Ludmilla A. Morozova-Roche, Jan Johansson, Sidong Xiong, Igor Iashchishyn, and Gefei Chen*

Amyloid fibrils—nanoscale fibrillar aggregates with high levels of order—are pathogenic in some today incurable human diseases; however, there are also many physiologically functioning amyloids in nature. The process of amyloid formation is typically nucleation-elongation-dependent, as exemplified by the pathogenic amyloid- β peptide (A β) that is associated with Alzheimer's disease. Spider silk, one of the toughest biomaterials, shares characteristics with amyloid. In this study, it is shown that forming amyloid-like nanofibrils is an inherent property preserved by various spider silk proteins (spidroins). Both spidroins and A β capped by spidroin N- and C-terminal domains, can assemble into macroscopic spider silk-like fibers that consist of straight nanofibrils parallel to the fiber axis as observed in native spider silk. While A β forms amyloid nanofibrils through a nucleation-dependent pathway and exhibits strong cytotoxicity and seeding effects, spidroins spontaneously and rapidly form amyloid-like nanofibrils via a non-nucleation-dependent polymerization pathway that involves lateral packing of fibrils. Spidroin nanofibrils share amyloid-like properties but lack strong cytotoxicity and the ability to self-seed or cross-seed human amyloidogenic peptides. These results suggest that spidroins' unique primary structures have evolved to allow functional properties of amyloid, and at the same time direct their fibrillization pathways to avoid formation of cytotoxic intermediates.

1. Introduction

The amyloid world hypothesis of the origin of life posits that peptide amyloids, which were effective against harsh conditions, were the first molecular entities that were able to self-replicate, transmit information, and evolve.^[1] In recent decades, amyloid nanofibrils have been extensively studied and identified as highly ordered, straight, and unbranched fibrillar polypeptide aggregates with a diameter of approximately 10 nm, consisting of β -strands that are oriented perpendicular to the fibril axis.^[2] Although amyloid is pathogenic and associated with around fifty human diseases, such as Alzheimer's disease (AD), Parkinson's disease (PD), and type 2 diabetes (T2D),^[2,3] non-pathological functional amyloid(-like) nanofibrils with well-defined physiological roles have been widely identified in natural species, including invertebrates (e.g., insects,^[4] spiders^[5]) and also bacterial biofilms^[6] and human (e.g., p-mel and some polypeptide hormones^[7]). According to the AmyPro database,^[8] characterized

X. Qi, H. Yu, R. Liu, H. Wang, S. Xiong
The Jiangsu Key Laboratory of Infection and Immunity
Institutes of Biology and Medical Sciences
Soochow University
Suzhou 215123, China

Y. Wang, Z. Zheng, Z. Jin, J. Johansson, G. Chen
Department of Biosciences and Nutrition
Karolinska Institutet
Huddinge 14157, Sweden
E-mail: gefei.chen@ki.se

Y. Wang
College of Wildlife and Protected Area
Northeast Forestry University
Harbin 150040, China

A. Leppert, M. Landreh
Department of Microbiology
Tumor and Cell Biology
Karolinska Institutet
Solna 17165, Sweden

Z. Zheng, Z. Jin
Department of Pharmacology
Xi'an Jiaotong University
Shaanxi 710061, China

X. Zhong
School of Engineering Sciences in Chemistry
Biotechnology and Health
Department of Biomedical Engineering and Health Systems
KTH Royal Institute of Technology
Huddinge 14152, Sweden

 The ORCID identification number(s) for the author(s) of this article can be found under <https://doi.org/10.1002/small.202304031>

© 2023 The Authors. Small published by Wiley-VCH GmbH. This is an open access article under the terms of the Creative Commons Attribution License, which permits use, distribution and reproduction in any medium, provided the original work is properly cited.

DOI: 10.1002/small.202304031

pathogenic and functional amyloids account for 36% and 43%, respectively, of total amyloids. Amyloid formation is often considered to be a nucleation–elongation-dependent process, where fibril growth requires the formation of an oligomeric nucleus, and fibril formation could be facilitated by the addition of preformed aggregates (seeding effects).^[9] Typical examples of this aggregation mechanism are pathogenic AD associated amyloid- β (A β) peptide^[10] and T2D relevant islet amyloid polypeptide (IAPP).^[11] The bacteria derived functional amyloid protein CsgA, the major building block of curli, also follows this nucleation-dependent aggregation pathway.^[12] Amyloidogenic aggregation from monomers has been also considered to follow the non-nucleation dependent isodesmic (or linear) polymerization pathway, where the association constants for monomer addition to any protein species are identical.^[9]

Insect and spider silk exhibit distinct structural features and are fascinating subjects for biomimicry. Interestingly, certain insect silk shares structural characteristics with amyloid nanofibril, for example, *Chrysopa flava* egg-stalk silk adopts a β -sheet rich structure in which several sheets associate to form a fiber with β -strands running perpendicular to the fiber axis.^[13] Spider silk, on the other hand, is one of the strongest biomaterials,^[14] and its mechanical strength and extensibility are determined by β -sheet nanocrystallites that are parallel to the fiber axis, in contrast to amyloid nanofibrils, as well as non-crystalline amorphous regions.^[15] Spider silk is made of many nanofibrils secreted by the spinneret on the posterior portion of the spider's abdomen consisting of millions of nanoscale tubes,^[16,17] holding amyloid-like characteristics. For instance, nanofibrils with diameters of 5–10 nm have been found in the spinning gland secretory vesicles of brown recluse spiders *Loxosceles laeta*^[18] and at the end of the silk production pathway of orb web spider *Trichonephila edulis*.^[5] Moreover, in natural spider silk fibers, nanofibrils with diameters ranging from several to hundreds of nanometers have also been reported.^[16] The ribbon-shaped silk of *L. laeta* contains numerous fine filaments that frequently assemble in pairs to generate a nanofibril with a diameter of ≈ 12 nm, which are orientated almost parallel to the long axis of the ribbon.^[18] For cylindrical silk fibers, a skin–core organization and functional coatings on top of the skin layer were identified for the major ampullate silk, and nanofibrils with diameters of ≈ 6 –17 nm in the core and ≈ 17 –100 nm in skin layer were described for different spider species to be parallel to the fiber axis.^[16,19–26] A recent study has shown that both major and minor ampullate silk fibers from the orb-web spi-

der *Nephila Madagascariensis* consist of nanofibrils arranged parallel to the long axis of the silk. The diameters of these nanofibrils are $145 \text{ nm} \pm 18 \text{ nm}$ and $116 \text{ nm} \pm 12 \text{ nm}$ for major and minor ampullate silk, respectively, spanning the entire length of the silk fiber.^[27] In addition to the ampullate silks, parallel nanofibrillar structures are also present in the egg sac silk of *T. edulis*.^[28]

There is also supporting evidence indicating the presence of nanofibrils in recombinant spider silk-like fibers.^[29,30] And interestingly, recombinant module tandems created from the low-complexity repetitive region of spider silk proteins (spidroins), or the terminal domains can assemble into nanofibrils in vitro when triggered by additives such as potassium phosphate or an acidic pH. Recombinant spidroin protein, comprising sixteen repeats of the module C derived from the orb web spider *Araneus diadematus* eADF-4 (major ampullate spidroin 2 (MaSp2) derivative), when induced by potassium phosphate, assembled into nanofibrils that bind amyloid-specific dyes Thioflavin T (ThT) and Congo Red.^[31–33] The short dodecapeptide from the silk β -sheet sequence of orb web spider *Araneus ventricosus* can self-assemble into 20 nm wide nanofibrils after incubation for 72 h in 5 mmol L^{-1} NaCl and 10 mmol L^{-1} phosphate buffer solution (PBS).^[34] The globular N- and C-terminal domains (NT and CT) play vital roles in regulating spider silk formation,^[14] in vitro experiments demonstrated that the non-repetitive CTs of *A. ventricosus* minor ampullate silk protein (MiSp) and flagelliform spidroin (FlSp) could spontaneously unfold and assemble into ThT-positive nanofibrils under acidic conditions,^[35,36] while the recombinant NT from *Euprosthenois australis* MaSp1 forms nanofibril-based hydrogel.^[37] While there are notable similarities between amyloid fibrils and spider silk fibrils, such as their comparable diameters, morphology, and the ability to bind amyloid-specific dyes, it is essential to acknowledge the formal definition of amyloid fibrils, which hinges upon an ordered cross- β -sheet structure within the fibrillar core, leading to a fibrillar architecture.^[2] In contrast, spider silk fibers exhibit a more intricate and diverse mixture of structures, encompassing both β -sheet crystalline regions and amorphous regions within the fibers.^[38] The same problem remains also in the amyloid field, when α -helical proteins form amyloid fibrils and there are indications that not all amino acid residue sequence form β -sheet and some remaining α -helices or nonstructured regions form the fibrillar interface.^[39,40] Considering the visual and inherent similarities between the nanofibrils derived from spidroins and amyloid fibrils, we have chosen to use the term “amyloid-like fibrils” in this study. This terminology acknowledges the shared characteristics and appearance of the spidroin-derived nanofibrils with amyloid fibrils, while recognizing the structural differences resulting from the heterogeneous nature of spider silks. By referring to the nanofibrils derived from spidroins as amyloid-like fibrils, we aim to highlight the resemblances while being mindful of the divergence from the precise definition of amyloid fibrils due to the complex structuring exhibited by spider silks. This designation allows us to effectively describe the observed features and properties of the nanofibrils in relation to the well-established amyloid paradigm.

Biomimetic spider silk-like fibers currently cannot compete with natural silks in terms of mechanical performance due to a lack of detailed understanding of the hierarchical structures of both natural and biomimetic spider silk fibers. While the

X. Li
Department of Pharmacology
College of Pharmacy
Chongqing Medical University
Chongqing 400016, China

X. Wang
Department of Neurology
Shanghai Sixth People's Hospital
Shanghai Jiao Tong University School of Medicine
Shanghai 200233, China

L. A. Morozova-Roche, I. Iashchishyn
Department of Medical Biochemistry and Biophysics
Umeå University
Umeå 90187, Sweden

micelle theory^[41] and liquid crystalline theory^[42] have been proposed to explain how spidroins rapidly form solid nanofibril-bundle-constituted silk fibers from highly concentrated soluble spidroins, the assembly mechanism is still to be established. Recently, it has been demonstrated that liquid-liquid phase separation (LLPS) occurs in response to multivalent anions mediated by the C-terminal and repetitive domains. Under mild acidification together with the LLPS conditions, recombinant MaSp2 variant rapidly self-assembled into dense nanofibrillar networks oriented along the longitudinal axis.^[43] Taken together, spider silks share common characteristics to amyloid nanofibrils that might play important roles in macroscopic silk fiber formation and the ultimate performance, yet the molecular mechanistic details are still to be elucidated, including how spidroins assemble into amyloid-like nanofibrils and subsequent macroscopic fibers. Moreover, it remains unknown whether these constituent amyloid-like nanofibrils are cytotoxic and possess cross-seeding effects on pathogenetic human amyloidogenic peptides, which is important when fibers are implemented for biomedical applications. Herein, we unraveled assembly mechanisms from spidroins to nanofibrils, evaluated the cytotoxicity and self/cross-seeding capacities, and performed comprehensive analyses on amyloid forming properties of different spidroins. The results provide general insights into the assembly of silk proteins and their biocompatibility.

2. Results and Discussion

2.1. Recombinant Spidroins Rapidly and Spontaneously Form Amyloid-Like Nanofibrils

Recombinant production of full-length spidroins dominated by repetitive regions is generally not feasible due to their large size. Therefore, truncated spidroins that represent characteristic repetitive patterns are commonly used.^[14] We have been focusing on a truncated repetitive region (amino acid sequence in Table S1, Supporting Information), Rep_{MiSp}, from the *A. ventricosus* spider MiSp.^[44] This region contains the typical MiSp motif Gly-Ala, accounting for 49% (Gly) and 36% (Ala), respectively (Figure 1a). Surprisingly, the recombinant Rep_{MiSp} could not stay in its soluble state. After one day of incubation at 4 °C in 20 mM Tris pH 8.0, there was a significant reduction in band intensity (Figure 1b). At room temperature, the reduction in the band intensity was even more noticeable and most of the Rep_{MiSp} proteins disappeared within one day incubation (Figure 1b). Although the reduction of the band intensity during incubation was rapid and pronounced at room temperature, no clear manifestations for solid precipitations or degradation during the incubation were observed. This phenomenon suggested that aggregates with ultrastructure probably formed, as it has been shown that recombinant spidroins consisting of eADF-4 repetitive module tandems have the ability to assemble into amyloid-like nanofibrils initiated by potassium phosphate.^[31,32] As predicted by the ArchCandy program that estimates the likelihood of a given amino acid sequence to form amyloid using the structural definition of amyloid,^[45] notably, Rep_{MiSp} displayed a high propensity to form amyloid nanofibrils (Figure 1c), supporting ultrastructure formation of recombinant Rep_{MiSp}.

To confirm that the recombinant Rep_{MiSp} formed highly structured aggregates, we imaged the products incubated at room temperature by transmission electron microscopy (TEM). A significant amount of nanoscale fibrils was observed with an average diameter of 16.6 ± 4.3 nm (Figure 1d,e), which falls within the amyloid fibril diameter range.^[47,48] Monitored by the ThT fluorescence assay, the recombinant Rep_{MiSp} followed a ThT-positive increase during the incubation time course (Figure 1f), indicating the formation of ThT-positive nanofibrils. Taken together, these results suggest the truncated MiSp spidroin Rep_{MiSp} can spontaneously assemble into amyloid-like nanofibrils in a normal physiological-like buffer at pH 8.0, most importantly, without any additives and shearing force. It has been shown that, to trigger fibril-formation, several independent physical and chemical conditions, that is, shear, reduction of pH, Na⁺, and Cl⁻ concentrations, need to be met simultaneously, and the absence of any of these triggers prevents premature assembly of spidroin in the storage sack, enabling long-term storage.^[49] We also tested the amyloid-like fibril formation of the recombinant Rep_{MiSp} in 20 mM Tris pH 8.0 in the presence of 150 mM NaCl under quiescent condition, and similarly, ThT-positive increase was observed (Figure S1, Supporting Information), suggesting recombinant MiSp spidroins can spontaneously assemble into amyloid-like nanofibrils without a decrease in pH or NaCl concentration and shearing force in vitro.

2.2. Forming Amyloid-Like Nanofibrils Is an Intrinsic Feature Preserved by Different Spidroins

Spiders produce a variety of proteinaceous silk fibers, such as MaSp, MiSp, FlSp, aciniform spidroin (AcSp), tubuliform spidroin (TuSp), and pyriform spidroin (PySp), each with unique mechanical properties suitable for diverse biological applications.^[14] The amyloidogenic nature of Rep_{MiSp} raised the question of whether other spidroins also possess this property. Different spidroins are predominantly composed of repetitive motifs/domains flanked by relatively conserved globular NT and CT.^[50] For instance, MaSp1 contains GGX, GX, and poly-A motifs, while MaSp2 consists of GPX, QQ, GGX, GSG, and poly-A motifs.^[51] The MiSp sequence is primarily comprised of Gly and Ala residues organized into GX, GGX, GGGX, and short poly-A repeats,^[44] and FlSp is rich in GPGGX motifs.^[52,53] Differently, AcSp, TuSp, and PySp do not follow the same repetitive pattern as the Gly-rich spidroins but contain non-Gly-rich repetitive domains, approximately 200 amino acid residues in length.^[54–56] Based on the amino acid composition and the size of the repetitive regions, the spidroins were grouped into Gly-rich (MaSp, MiSp, and FlSp) and non-Gly-rich (AcSp, TuSp, and PySp) categories (Figure S2, Supporting Information).

To investigate the amyloid-forming properties of various types of spidroins, the full-length amino acid sequences were subjected to amyloidogenicity prediction individually using ArchCandy (Figures S3–S6, Supporting Information). Surprisingly, the repetitive regions of the non-Gly-rich group, that is, AcSp, TuSp, and PySp, all displayed high amyloidogenic propensities with large β -arcade-forming patches (Figure 2a; Figures S5, S6, Supporting Information), which supports the presence of nanofibrils in native spider egg sac silk^[28] and apparently at

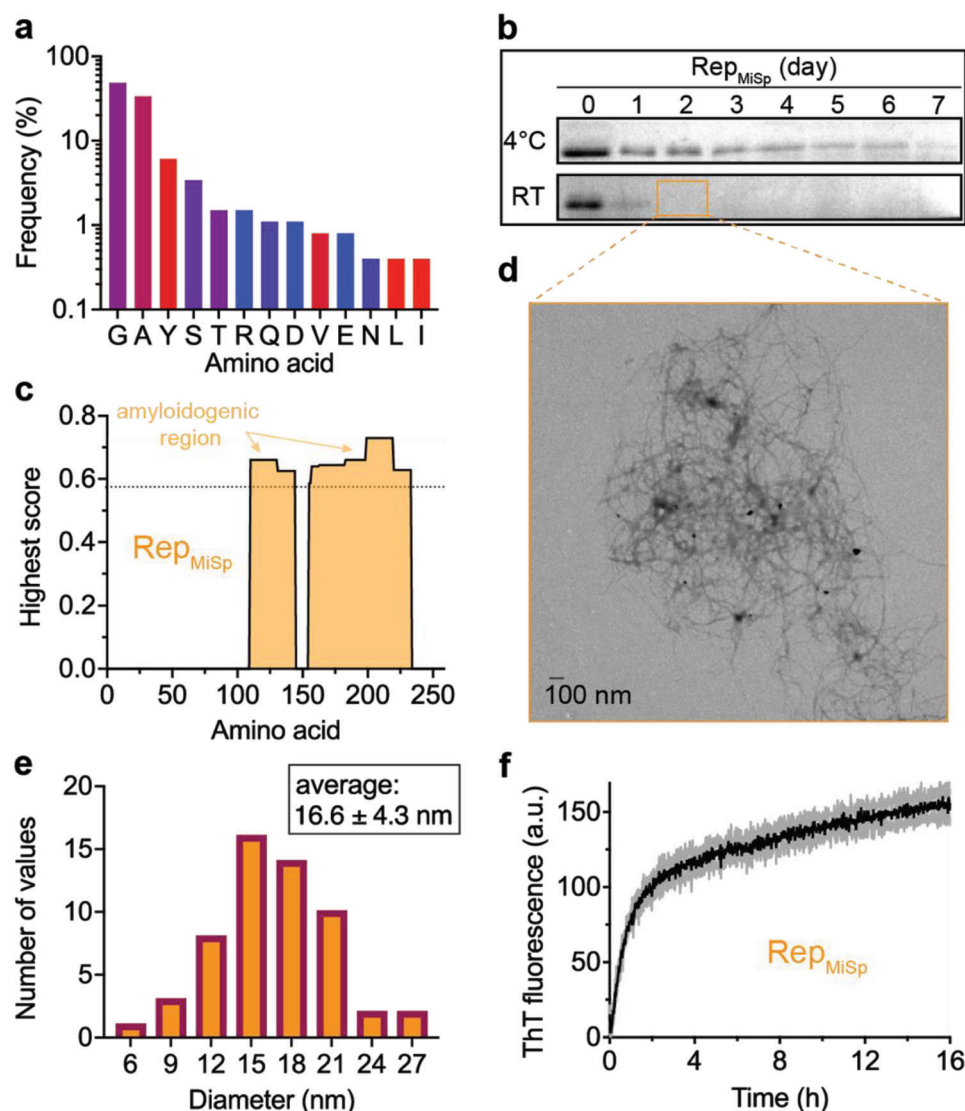


Figure 1. Amyloid-like nanofibril formation of recombinant spidroins Rep_{MiSp} derived from *A. ventricosus* MiSp repetitive region. a) Amino acid composition (%) of Rep_{MiSp}. The amino acids are shown in single letter format along the X-axis, while the Y-axis is the corresponding frequency (%). b) Stability analysis of recombinant Rep_{MiSp} by SDS-PAGE. The numeral numbers on top of the gels indicate the incubation time (day) at 4 °C and room temperature (RT), respectively. c) Rep_{MiSp} amyloidogenic region prediction by ArchCandy.^[45] The scoring threshold 0.575 is indicated by the dash line. d) TEM image of Rep_{MiSp} after two days incubation at room temperature and e) diameter measurements of the subsequent amyloid-like nanofibrils were performed with Fiji.^[46] f) Fibril formation trace of 4.5 μM Rep_{MiSp} in 20 mM Tris pH 8.0 at 25 °C monitored by ThT assay under quiescent conditions. The shadow in gray along the trace represents standard deviations.

the ending point of recombinant spider silk-like fibers of AcSp repeats.^[57] In the Gly-rich group, MaSp1 and Flag repetitive regions did not display obvious regions for β -arcade formation (Figures S3b, S4b, Supporting Information), whereas the MiSp repetitive region exhibited many large areas capable of forming fibrillar β -arcades (Figure 2a; Figure S3a, Supporting Information). Despite being rich in prolines, small amyloidogenic regions were predicted to form fibrillar amyloid structures in the repetitive region of MaSp2 (Figure 2a; Figure S4a, Supporting Information), consistent with a previous study reporting that recombinant MaSp2 derivative eADF4 module repeats ($n \geq 2$) form amyloid-like nanofibrils in the presence of potassium phosphate.^[33] Notably and interestingly, ArchCandy predic-

tions indicated that most of the NTs and all of the CTs exhibited high amyloid-forming propensities, with significant β -arcade-forming regions (Figure 2b,c; Figures S3–S6, Supporting Information). The biological functions of amyloid fibril formation in the terminal domains remain unclear, but it has been experimentally confirmed in vitro that the recombinant CTs of MiSp and Flag form in a pH-sensitive manner amyloid-like nanofibrils that are thought to trigger the repetitive regions to rapidly form fibers, but seeding effects from these CT nanofibrils have not been reported.^[35,36]

Given the limitations of the ArchCandy prediction, such as its inability to predict stacking of anti-parallel β -arches or β -solenoidal structure,^[45] we used the AMYLPRED2 consensus

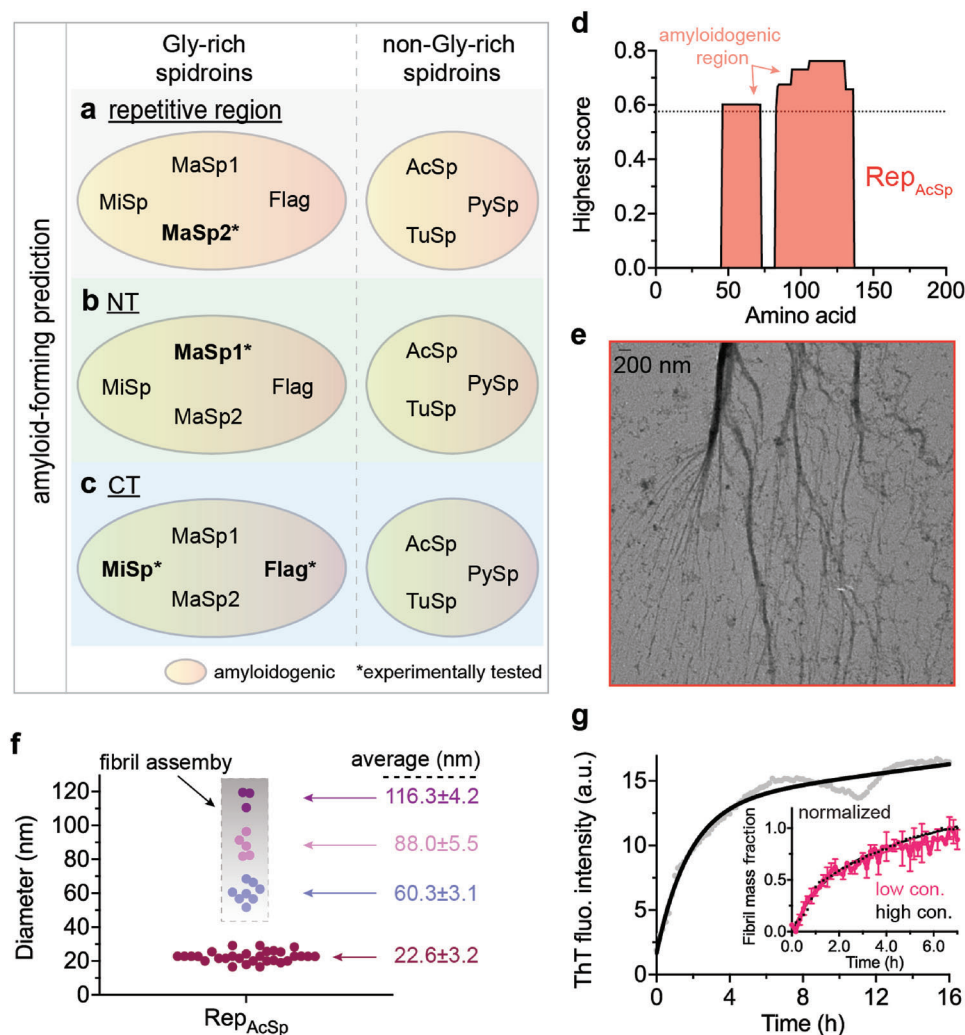


Figure 2. Amyloid formation analysis of different spidroins. a–c) Amyloid forming predictions of the full-length MiSp, MaSp1/2, Flag, AcSp, TuSp, PySp by ArchCandy and AMYLPRED2. The predictions for a) the repetitive regions, b) the NTs, and c) CTs are shown separately. The corresponding full predictions and relevant scores are shown in Figures S3–S9, Supporting Information. d) Amyloidogenic prediction of an AcSp repeat—Rep_{AcSp} by ArchCandy. The scoring threshold 0.575 is shown by the dash line. e) TEM image of Rep_{AcSp} after incubation at room temperature, and f) diameter measurements of the subsequent amyloid-like nanofibrils were performed with Fiji. g) Fibril formation traces of Rep_{AcSp} at two different concentrations (0.80 and 0.25 mg mL⁻¹) in 20 mM Tris pH 8.0 at 25 °C monitored by ThT assay under quiescent conditions. The inset shows the normalized traces.

method to predict amyloidogenic regions in spidroins that did not exhibit β -arcade patches in ArchCandy prediction, namely the repetitive regions of Flag and MaSp1 and the NTs of MiSp and PySp. Upon AMYLPRED2 prediction, the repetitive region of MaSp1 displayed amyloid-forming regions mainly located within the poly-A motifs (Figure 2a; Figure S7, Supporting Information), supporting the notion that the poly-A motifs are responsible for forming the β -sheet nanocrystallites present in spider major ampullate silk fibers.^[58] The short spacer motifs in spider species that spin Flag fibers containing β -sheets have a higher β -sheet propensity, but the long distance between the spacer motifs might not be compatible with the prediction of ArchCandy.^[45] According to the AMYLPRED2 consensus method, the short spacers of *A. ventricosus* Flag are the primary sites responsible for forming β -strands and further amyloid structures (Figure 2a; Figure S8, Supporting Information).

Similarly, the NTs from MiSp and PySp were also found to have many amyloid-forming patches (Figure 2b; Figure S9a,b, Supporting Information). These computational predictions suggest a potential common property of spidroins, including both the repetitive regions and the terminal domains, in their propensity for forming amyloid-like structures despite having strikingly different amino acid sequences. This finding is consistent with the presence of nanofibrils in natural spider silk fibers, which have been observed so far only in major ampullate silk, minor ampullate silk, and egg sac silk.^[16] However, these microscopic fibrillar structures are likely to differ, resulting in diverse structures and performance in the solid macroscopic silk fibers.

As the Rep_{MiSp} from the Gly-rich group showed strong amyloid-like fibril propensity, the prediction results led us to experimentally confirm the amyloid-forming propensities of spidroins from the non-Gly-rich group—the repeat Rep_{AcSp}

(amino acid sequence in Table S1, Supporting Information) derived from *A. ventricosus* AcSp. This truncated AcSp repetitive region has previously been shown to assemble into spider silk-like fibers by hand-pulling in 20 mM Tris pH 8.0 in the presence of terminal domains.^[59,60] ArchCandy prediction revealed that Rep_{AcSp} contains large amyloidogenic patches (Figure 2d). We produced recombinant Rep_{AcSp} proteins from *E. coli*, and under TEM Rep_{AcSp} nanofibrils with diameter of 22.6 ± 3.2 nm were observed after incubation (Figure 2e,f). Interestingly, these nanofibrils apparently assembled and packed together, further generating relatively thicker nanofibrils, from 60.3 ± 3.1 nm to 116 ± 4.2 nm (Figure 2e,f). Additionally, the recombinant Rep_{AcSp} showed a ThT-positive increase in 20 mM Tris pH 8.0 (Figure 2g), indicating the formation of ThT positive amyloid-like nanofibrils. Further, the recombinant Rep_{AcSp} also exhibited a similar aggregation pattern as Rep_{MiSp}, without lag phase and plateau (Figure 2g), and the traces at relatively low and high concentrations overlapped after normalization (Figure 2g inset), which suggested that Rep_{AcSp} assembles into nanofibrils following a mechanism comparable to Rep_{MiSp}.

2.3. Spidroins Assemble into Amyloid-Like Nanofibrils via a Non-Nucleation-Dependent Polymerization Pathway

Amyloid fibril formation is often a nucleation–elongation-dependent process; however, amyloidogenic aggregation also follows the non-nucleation dependent isodesmic (or linear) pathway.^[9] To gain further mechanistic characterizations of spidroin nanofibril formation, we focused on the Rep_{MiSp} that spontaneously forms ThT positive amyloid-like nanofibrils in a normal physiological-like buffer under quiescent condition. To synchronize the reaction, the recombinant spidroin Rep_{MiSp} was further refined by size exclusion chromatography (SEC) for monomer isolation, where a well separated monomer peak was eluted (Figure 3a). Circular dichroism (CD) measurements showed Rep_{MiSp} has a random coil conformation (Figure 3b), which transformed to β -sheet and β -turn along nanofibril formation, demonstrated by Fourier-transform infrared spectroscopy (FTIR) spectrum with shifted Amide I bands toward 1624 cm^{-1} and 1679 cm^{-1} (Figure 3b inset), similar to the fibrils formed by recombinant spidroin repeats of the eADF-4 (MaSp2 derivative) module C.^[32,33] The structure of spider silk crystalline areas has been proposed to be composed of β -sheets, with poly-Ala (for MaSp) or poly-Gly-Ala (for MiSp) forming the structure with successive alanine/glycine residues placed on alternate sides of a backbone. Interlocking of adjacent chains is achieved via hydrophobic interactions, with poly-Ala providing higher hydrophobicity than poly-Gly-Ala, thus reflecting the lower tensile strength of minor ampullate silk compared to major ampullate silk.^[58] The program—BetaSerpentine—predicts possible β -serpentine arrangements of adjacent β -arches that could be estimated by the ArchCandy program,^[45] and has been used to accurately predict the amyloid structure arrangement of, for example, A β 42 and α -synuclein with a good agreement to the corresponding Nuclear magnetic resonance (NMR) data.^[61] Within Rep_{MiSp} from pos. G109 to G234 (Figure 1c; Table S1, Supporting Information), BetaSerpentine was able to establish a consensus arrangement of ten significant β -strands (Figure S10a, Supporting

Information). The representative β -serpentine showed that the poly-A motif, forming β -sheet crystalline areas in MaSp responsible for spider major ampullate silk tensile strength,^[51] as well as Gly/Ala motif in Rep_{MiSp} formed β -strands, and the Ala/Ala or Gly/Ala packing plays important roles on the β -serpentine arrangements (Figure S10b, Supporting Information), supporting the proposed structure of poly-Ala or poly-Gly-Ala in crystalline areas of spider silk. In *L. laeta* ribbon silk nanofibrils, β -sheets are the dominating secondary structure attributed to Gly and Ala, but helical structures including 3_1 -helices and α -helices also play significant roles.^[62] Beside the core amyloidogenic region of Rep_{MiSp}, there are regions rich in Gly and Ala that do not form β -arches (Figure 1c; Table S1, Supporting Information), suggesting they might be involved in the formation of other secondary structures.

To elucidate the underlying amyloid-like fibril forming mechanism, we conducted a series of ThT measurements on recombinant Rep_{MiSp} at varying initial monomer concentrations in 20 mM Tris pH 8.0 at 25 °C under quiescent conditions (Figure 3c). The final fluorescence intensity showed a linear relationship with the initial monomer concentration (Figure 3d), indicating that ThT accurately reports on the reaction progress within the given concentration range of the Rep_{MiSp} monomer, as previously reported for other amyloidogenic peptides.^[10,63] Notably, we observed neither stable plateau for any Rep_{MiSp} concentration within the testing time range nor typical lag phase, which suggested a non-nucleation-dependent polymerization mechanism.^[9] Upon data normalization, the aggregation traces of different Rep_{MiSp} concentrations overlap (Figure 3c inset), indicating the aggregation constants are not concentration dependent. Further, kinetic traces of Rep_{MiSp} have no inflection point (Figure 3c), indicating a polymerization reaction.

The distribution of filament masses showed a Poisson's shape (Figure 3e), which is indicative of chain polymerization.^[64] If monomer fraction serves as initiator, first exponential decay can be ascribed to polymerization. Using living polymerization formalism initiator concentration can be calculated from the distribution via:

$$L_{av} = 1 - M_0/I_0 \quad (1)$$

where L_{av} —average filament length, M_0 —starting monomer concentration, and I_0 —initiator concentration. For linear polymers the distribution of masses is the same as the distribution of lengths. Average filament length according to mass photometry is ten monomers (Figure 3e), which gives the initiator concentration of 0.51 μM . It is an upper estimate, since fraction of monomers that serve as initiator decreases number of monomers (C_0) available for polymerization, that is, $M_0 = C_0 + I_0$.

The second exponential decay can be attributed to conformational change of the growing filaments. Spectroscopic analysis suggests that silk protein unfolds in multiple steps.^[65] Since the number of initiator monomers represent the number of filaments, then the conformation term is also proportional to I_0 . Therefore, the fitting model can be written as a sum of two terms—polymerization and conformational change:

$$F/F_\infty = C_0 e^{-k_i I_0 t} + (1 - C_0) e^{-k_c I_0 t} \quad (2)$$

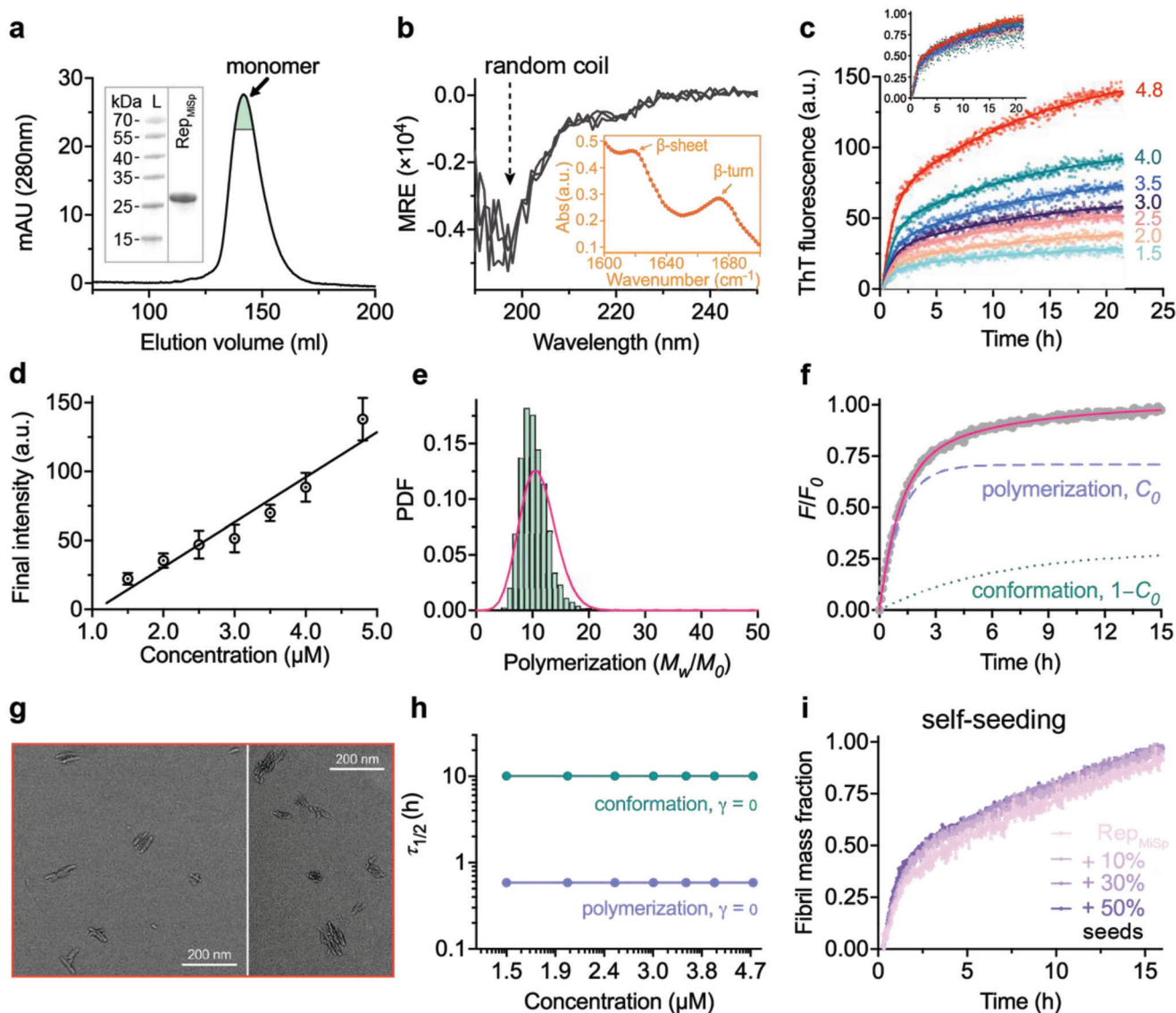


Figure 3. Mechanism investigation of Rep_{MiSp} nanofibril formation. a) Rep_{MiSp} monomers isolation by a superdex75 column connected to an äkta system. The green shadow is for the fraction collected, and the purity assessment by SDS-PAGE is as inset. Lane L is for protein ladder. b) Secondary structure measurements of soluble Rep_{MiSp} monomers and the nanofibrils by CD (three scans) at 25 °C and FTIR, respectively. Secondary structure evaluation of Rep_{MiSp} nanofibrils was measured by FTIR (inset). β -sheet and β -turn are arrow-labelled. c) Aggregation kinetics of Rep_{MiSp} at 1.5, 2.0, 2.5, 3.0, 3.5, 4.0, and 4.8 μ M in 20 mM Tris pH 8.0 at 25 °C under quiescent conditions. The normalized traces are shown as inset. The traces were globally fitted with a two phase exponential equation. d) Plot of the final intensities against concentrations of Rep_{MiSp} aggregation kinetics from (c), and a linear fitting was applied. e) Distribution of average molecular weights overnight incubated Rep_{MiSp} measured by mass photometry. M_0 is a molecular weight of the monomer (≈ 20 kDa). PDF in Y-axis is for probability density function. f) Normalized ThT fluorescence for 4.6 μ M (starting concentration) of Rep_{MiSp} (grey points) at 25 °C under quiescent condition. Polymerization term is shown by dash line (light blue), conformation term by dotted line (green), solid line (red) represents their sum. g) TEM microimages of overnight incubated Rep_{MiSp}. The scale bar is 200 nm. h) Logarithmic plot (log-log) of the reaction $\tau_{1/2}$ values extracted by sigmoidal fitting from (c) versus the initial monomer concentration of the recombinant Rep_{MiSp}. γ is for the slope. i) Fibril formation of 4.0 μ M Rep_{MiSp} in the presence of different concentrations of preformed Rep_{MiSp} nanofibrils in 20 mM Tris pH 8.0 at 25 °C under quiescent conditions.

where F and F_∞ are fluorescence intensity and fluorescence intensity at 200 h extrapolated from the double exponential decay fitting, C_0 —monomer concentration available for polymerization, I_0 —monomer concentration serving as initiator, k_t —polymerization rate, and k_c —conformational change rate. Before fitting data was normalized to F_∞ . Despite the good fitting of the kinetic trace (Figure 3f), the value of C_0 is less than the upper es-

timate of initiator concentration from the distribution. In other words, there is a mismatch between the concentration of initiator determined from distribution ($\approx 12\%$ of M_0) and kinetic traces ($\approx 30\%$ of M_0). Such difference is most likely related to assumptions of the complicated conformational changes due to polymerization.^[65] Upon polymerization of proteins the rate limiting step is conformational change, which requires additional

treatment. Furthermore, as indicated by TEM microscopic images, Rep_{MiSp} was able to form single short amyloid-like fibrils, which then packed together side-wise (Figure 3g). This phenomenon provided a mechanistic explanation for how relatively thicker nanofibrils with a diameter from few to hundred nanometers form in mature fibers.

To find out the aggregation constant rates, the aggregation traces of different concentrations of Rep_{MiSp} were fitted globally, and they were described well with the two-term exponential model (Equation (2)) (Figure 3c,f), while k_p is $5.0 \times 10^{-10} \text{ M}^{-1} \text{ s}^{-1}$ and k_c is $0.88 \times 10^{-10} \text{ M}^{-1} \text{ s}^{-1}$. The dependence of reaction half-time ($\tau_{1/2}$) values on the concentration of spidroin Rep_{MiSp} gave straight flat lines for both the polymerization and conformation change half-times, indicating the aggregation half-times were not Rep_{MiSp} monomer concentration dependent (Figure 3h). For the nucleation-polymerization model the slope of a log–log plot of the reaction $\tau_{1/2}$ values versus the initial monomer concentration equals half of the critical nucleus size (n)— $n/2$.^[66] In case of the fibrillization of the recombinant Rep_{MiSp}, kinetics of fibrillization did not show a high-order dependence on the spidroin monomer concentration, indicating no oligomeric nucleus forms. This mechanism was further confirmed by the seeding experiments, which showed that no self-seeding capacity is present for Rep_{MiSp} fibrils, indicated by the overlapped aggregation kinetics with and without different concentrations of preformed Rep_{MiSp} nanofibrils (Figure 3i). This specific non-nucleation dependent fibril polymerization mechanism is different from the previously reported fibrillization mechanism. Further, to find out whether this polymerization mechanism applies to the amyloid-forming spidroin terminal domains, we performed a series of ThT measurements on recombinant MiSp C-terminal domain that has shown the ability to form amyloid-like fibrils under acidic conditions.^[35,67] Interestingly, the aggregation pattern of MiSp CT was similar to that of the Rep_{MiSp}. The overlapping normalized traces indicated the aggregation constants are not concentration independent, and the aggregation traces of different concentrations of MiSp CT were fitted well globally with the two-phase exponential model (Figure S11, Supporting Information), suggesting the above non-nucleation polymerization mechanism also applies to the MiSp CT fibril formation. So far, the only reported recombinant spidroin containing sixteen repeats of the module C of *A. diadematus* eADF-4 (MaSp2 derivative), triggered by potassium phosphate, followed the nucleation and elongation pathway to assemble into amyloid-like nanofibrils with seeding effects.^[33,68] This discrepancy could be due to different spidroin types (i.e., amino acid compositions) or the different fibril preparation conditions as the nanofibrils of recombinant eADF-4 tandem were triggered by potassium phosphate.^[68]

2.4. Cross-Seeding Effects and Cytotoxicity of Rep_{MiSp} Nanofibrils

Amyloid fibrils have been discovered to be cross-seeding active,^[69] a biological event where one type of protein's amyloid structure (homologous amyloids) can act as a seed and facilitate the aggregation of another amyloid protein, leading to the formation of heterologous amyloids. However, not all amyloid proteins can cross-seed each other, implying the existence of a cross-seeding barrier. Silk fibrils from the cocoon of *Bom-*

byx mori, Sup35 fibril from *Saccharomyces cerevisiae*, and curli fibril from *E. coli* exert amyloid-accelerating properties in the murine experimental AA amyloidosis, suggesting that such factors may be important risk factors in amyloidogenesis.^[70] To investigate whether the Rep_{MiSp} amyloid-like nanofibrils can cross-seed pathogenic peptide although it did not show self-seeding effects, we recombinantly prepared the AD associated A β 42 (42 amino acid residues), the most aggregation prone and toxic variant of A β , and monitored the amyloid fibril formation with and without different concentrations of preformed Rep_{MiSp} nanofibrils. It is worth mentioning that the A β 42 peptide is extremely active, and can be self-seeded (also see below) and cross-seeded by different preformed fibrils,^[69] including cattle meat (human consumable) extracted AA fibrils.^[71] Interestingly, the fibrillization traces of A β 42 with and without preformed Rep_{MiSp} amyloid-like fibril seeds were able to be superimposed, and the aggregation half time $\tau_{1/2}$ and maximum aggregation rate r_{max} both showed approximately flat lines, even with up to 40% (of the A β 42 monomer molar concentration) of seeds (Figure 4a,b), indicating no cross-seeding effects, which is different from the above mentioned fibrillar materials as well as the eADF-4 (MaSp2 derivative) fibrils.^[33,68] The aggregation in cross-seeding results from intermolecular interaction between different proteins, especially oppositely charged proteins. The heterologous amyloids provide an electrostatically favorable environment and exposition of partially hydrophobic surfaces. These hydrophobic surfaces further trigger the nucleation and growth of aggregates.^[69] The charged amino acid content in Rep_{MiSp} is low (Figure 1a), which may explain why cross-seeding effects are undetectable. These results suggest the spidroin Rep_{MiSp} can form amyloid-like fibrils through a non-nucleation-dependent aggregation pathway, and the lack of self-seeding and cross-seeding capacity might suggest the intrinsic structure of spider silk is biocompatible for various biomedical applications.

Many amyloids are pathogenic and associated with different severe diseases, e.g., the neurodegenerative disease.^[2,3] Silk nanofibrils and nanofilaments, which are composed of β -sheets, have been recently reported to be not significant cytotoxic to in vitro neuronal cells.^[72] Nanofibrils of the short dodecapeptide from *A. ventricosus* spider silk β -sheet sequence did not present significant cytotoxicity to rat pheochromocytoma (PC12) cells, suggesting peptides composed of Gly and Ala do not express significant cytotoxicity likely because of the lack of surface charges on the peptide assemblies.^[34] To investigate the pathogenic properties of the Rep_{MiSp}-based materials, we assessed the abilities to generate toxic responses to different cell lines. Both soluble Rep_{MiSp} and the nanofibrils at concentrations of 50, 100, and 250 $\mu\text{g mL}^{-1}$ were evaluated for cytotoxicity against different cancer cell lines, that is, HeLa and HT29 via the CCK-8 Cell Proliferation Assay Kit, respectively (Figure 4c,d). The soluble Rep_{MiSp} and the nanofibrils at lower concentrations, that is, 50 and 100 $\mu\text{g mL}^{-1}$, did not show significant cytotoxicity to either cell line, whereas at concentration of 250 $\mu\text{g mL}^{-1}$, weak cytotoxicity was detected (Figure 4c,d), in line with observations for the amyloid-like nanofibrils from the dodecapeptide.^[34] These results suggested that Rep_{MiSp} fibrils are not significantly cytotoxic to human cancer cell lines. To find out whether the cytotoxicity of Rep_{MiSp} is dependent on its assembly states, triggered by potassium phosphate, the recombinant Rep_{MiSp} self-assembled into

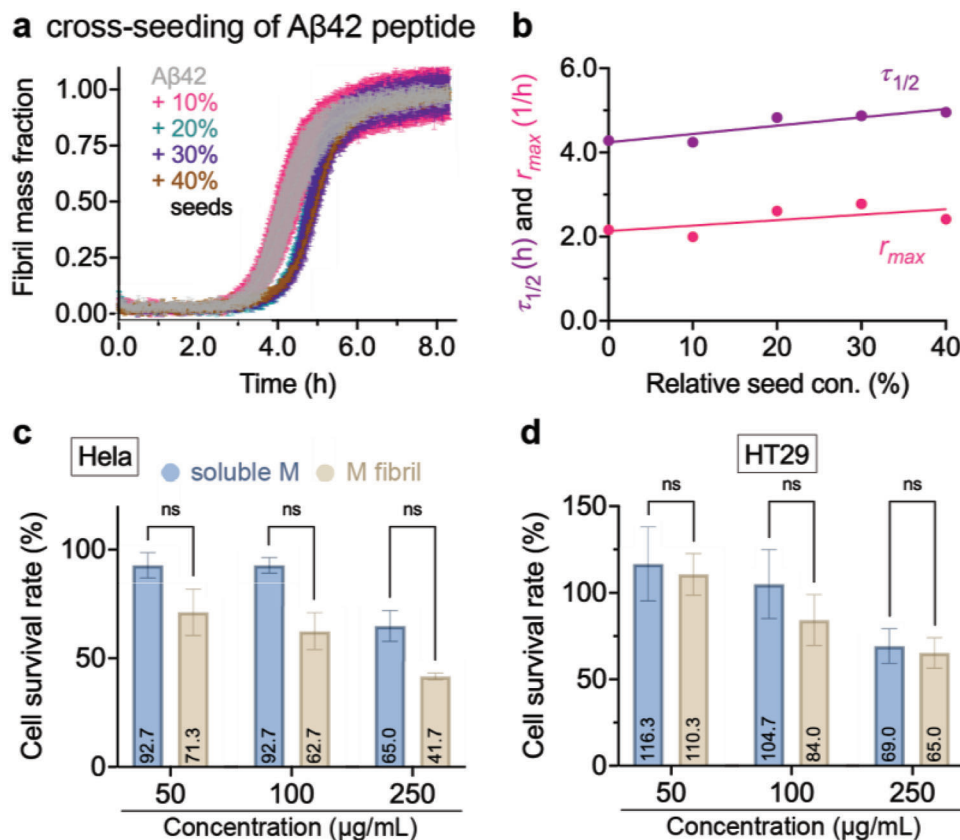


Figure 4. Cross-seeding and cytotoxicity evaluation of Rep_{MiSp} proteins and nanofibrils. a) ThT assay of fibrillization of 2.0 μmol L⁻¹ Aβ42 monomers in the presence of different concentrations, that is, 0%, 10%, 20%, 30%, 40% (of 2.0 μmol L⁻¹ Aβ42) of preformed Rep_{MiSp} nanofibrils. b) The half time ($\tau_{1/2}$) and maximum aggregation rate (r_{max}) were extracted by sigmoidal fitting. Both soluble Rep_{MiSp} and Rep_{MiSp} nanofibrils at concentrations of 50, 100, and 250 μg mL⁻¹ were evaluated for cytotoxicity against different cancer cell lines, that is, c) HeLa, and d) HT29, via the CCK-8 assay, respectively. ns, no significance. Data are presented as mean ± SD.

nanoparticles in the presence of 2 mol L⁻¹ potassium phosphate (Figure S12a,b, Supporting Information) followed by cytotoxicity evaluation. Under scanning electron microscope (SEM), these nanoparticles were apparently spheric and homogeneous, and presented smooth surface, with diameter mainly from 350–600 nm (Figure S12c, Supporting Information), which is comparable to that of the nanoparticles formed by other customized spidroins.^[68,73] The Rep_{MiSp} nanoparticles were evaluated for cytotoxicity against HeLa cell lines and did not present obvious cytotoxicity evaluated by CCK-8 assay at the testing concentrations from at 50–250 μg mL⁻¹ (Figure S12d, Supporting Information), indicating the nano assemblies of recombinant Rep_{MiSp} are not obviously cytotoxic, probably due to its amino acid composition.

2.5. Both Spidroin and Pathogenic Amyloid Peptide Can Form Silk-Like Fibers

Inspired by the intrinsic amyloid-like nanofibril forming propensity of spidroins, we focused on the Rep_{MiSp} to investigate whether it possesses general spider silk-formation propensity as the full-length silk protein and to see whether the nanofibril-like microstructure could be present in macroscopic fibers. As such, the spidroin Rep_{MiSp} was expressed with its native N-terminal

domain (NT_{MiSp}, referred to as N) and the C-terminal domain from flagelliform silk protein (CT_{FLiSp}, referred to as C), generating a chimera protein N-Rep_{MiSp}-C. Interestingly, the recombinant chimera protein N-Rep_{MiSp}-C produced from *E. coli* was able to assembly into silk-like fibers in 10 mM Tris pH 8.0 via manually hand-pulling (Figure 5a). Moreover, the resulting N-Rep_{MiSp}-C silk-like fibers exhibited sufficient autofluorescence at 405 nm excitation under conventional confocal microscopy, allowing visualization of a microfibrillar texture. Notably, the macroscopic silk-like fibers present bundle-like assembly, that is, the fibers consist of many thin fibrils bundled together (Figure 5b–d). The fibrillar arrangement of the silk was clearly visible, with nanofibrils accurately oriented along the axis of the fiber, and many nanofibrils clearly following the entire length of the fiber (Figure 5b–d), similar to the native MiSp ampullate silk that contains nanofibrils parallel to the long axis of the silk.^[27] Nonfluorescent areas were also observed, as previously described in other native silks.^[28] Previous research has shown that the recombinant AcSp repeat from *A. trifasciata* can form silk-like fibers, with the tail end of the fiber showing numerous smaller fibrils, suggesting that the nanofibrils may amalgamate together to form spider silk fibers.^[57] Recently, natural major ampullate silk fibers from the golden silk orb-weaver *Trichonephila clavipes* were decomposed into ≈10 nm-diameter nanofibrils with identical morphologies,

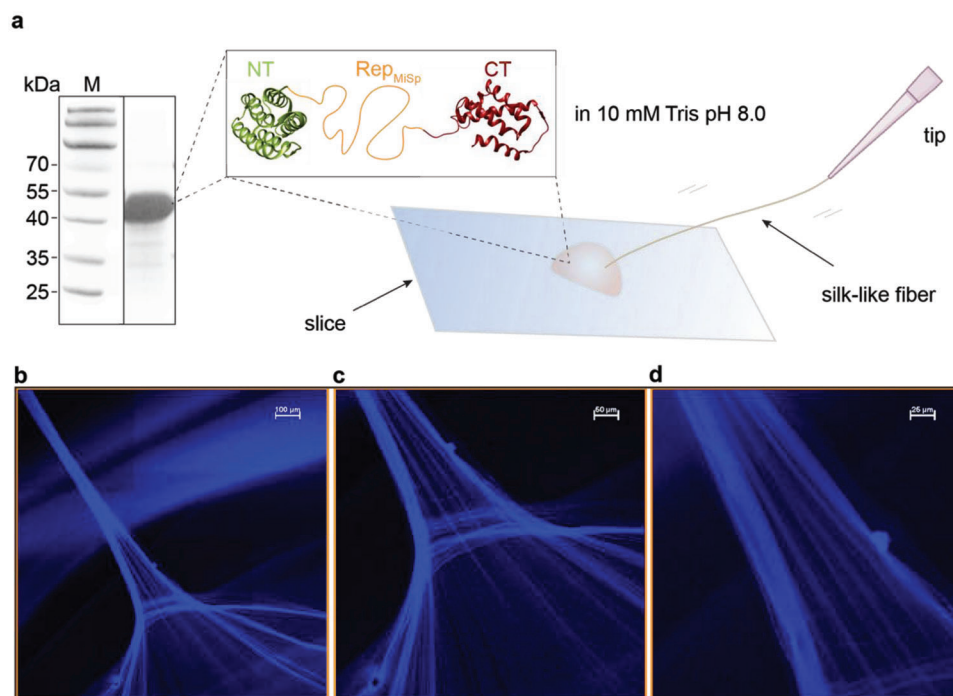


Figure 5. Spider silk-like fiber formation by NT-Rep_{MiSp}-CT. a) Schematic illustration of silk-like fiber generation by hand-pulling. A drop of protein solution in 10 mM Tris pH 8.0 was placed on a glass slice and the fiber was pulled out with a tip at a constant rate roughly. The purity of NT-Rep_{MiSp}-CT was assessed by SDS-PAGE. M is for protein marker. b–d) Imaging of NT-Rep_{MiSp}-CT silk-like fibers by confocal microscopy at different magnifications. The silk-like fiber was pulled from bottom to top direction. The scales bars are 100 μm, 50 μm, and 25 μm, respectively, from left to right.

and nanofibrils were also synthesized with almost identical morphology through self-assembly from native silk dope. Even at neutral pH in PBS, the dope formed clusters of short protein fibril segments with diameters of ≈ 10 nm.^[49] Our results suggest that the amyloidogenic spidroin Rep_{MiSp} retains the capability to assemble into solid spider silk-like fibers, which are made up by nanofibrils amalgamated together along the silk-like fiber axis, and this architecture probably represents the microscopic constituents of native spider silk.

Although a growing body of evidence suggests that amyloid structure is widespread in nature for beneficial purposes, termed functional amyloids, there are quite many protein misfolding phenomenon that leads to amyloid deposition primarily associated with neurodegenerative diseases.^[47] The typical example is the A β peptide, which forms amyloid fibrils and initiates AD developments.^[74] The kinetics of A β 42 aggregation is typically described by a nucleation-dependent polymerization model that is different from the linear polymerization (Figure 6a):^[47] monomers associate and form a nucleus (primary nucleation), from which a fibril can start to elongate (elongation); monomers attach to the surface of a fibril that catalyzes the formation of a new nucleus and leads to exponential fibril growth. This secondary nucleation autocatalytic pathway is the predominant source of toxic A β 42 oligomers.^[10] Different from Rep_{MiSp} fibril formation, A β 42 fibrillization showed a strong concentration dependent pattern monitored by the ThT fluorescence assay (Figure 6b); however, similar to the amyloid-like fibril forming Rep_{MiSp}, A β 42 formed nanofibrils with a diameter of ≈ 15 nm (Figure 6c inset). A β 42 fibrils possessed very strong

self-seeding effects, with only 6 nmol L⁻¹ preformed A β 42 fibrils as seeds, monomeric A β 42 fibril forming kinetics were accelerated (Figure 6c). And the preformed A β 42 fibrils showed obvious cross-seeding effects and promoted the fibril formation of recombinant tau proteins linked to AD (Figure 6d), and other human proteins/peptides, including T2D associated IAPP, PD relevant α -synuclein.^[69] To investigate whether the pathogenetic amyloid peptide, following the nucleation-dependent fibril formation pathway, can assemble into silk-like fibers similar to spidroins that aggregate into amyloid-like nanofibrils via a non-nucleation dependent pathway, the A β 42 was fused with the NT_{MiSp} and CT_{FISp}, generating a chimera protein N-A β 42-C. The chimera protein was expressed in *E. coli* with good yield and purified by immobilized metal affinity chromatography to high purity (Figure 6e). Interestingly, like the recombinant N-Rep_{MiSp}-C proteins, the recombinant chimera protein N-A β 42-C was also able to assemble into protein fibers in 10 mM Tris pH 8.0 via manually hand-pulling (Figure 6f), and no macroscopic fibers were observed in the absence of the terminal domains. Similar to the N-Rep_{MiSp}-C spider silk-like fibers, nanofibrillar texture of these fibers also present bundle-like compositions with oriented along the axis (Figure 6f). The intrinsic fluorescence for N-A β 42-C fibers was much weaker than that of the N-Rep_{MiSp}-C, which is attributed to the difference in primary structures between A β 42 and Rep_{MiSp} (Table S2, Supporting Information). These results suggest that human pathogenic amyloid peptide can be incorporated into solid protein fibers consisting of parallel nanofibrils, when capped with the spidroin N- and C-terminal domains that are important for the regulation of spider silk formation.^[14,75]

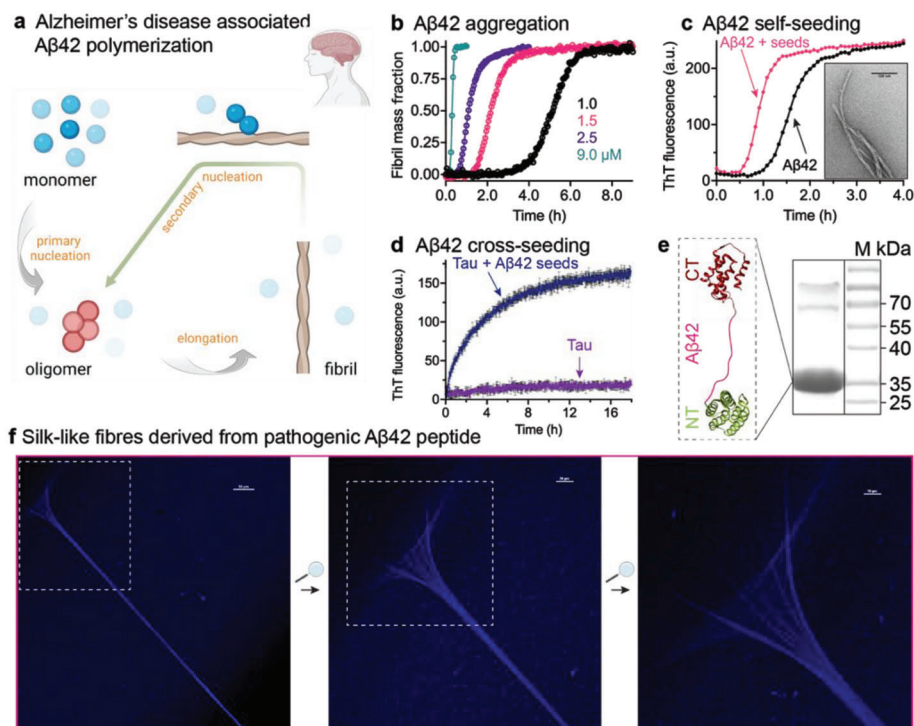


Figure 6. Silk-like fiber formation by NT-A β 42-CT. a) Schematic illustration of the aggregation mechanism of AD relevant A β 42 peptide. Monomers associate and form a nucleus (primary nucleation), from which a fibril can start to elongate (elongation); monomers attach to the surface of a fibril that catalyzes the formation of a new nucleus and leads to exponential fibril growth. b) Normalized aggregation kinetics of A β 42 monomers at 1.0, 1.5, 2.5, and 9.0 μ M at 37 $^{\circ}$ C under quiescent conditions. c) Self-seeding of A β 42 fibrils. 3 μ M A β 42 monomer was incubated at 37 $^{\circ}$ C with and without 6 nm preformed A β 42 fibrils. The inset shows the representative A β 42 fibrils under TEM. d) Cross-seeding of A β 42 fibrils. 3 μ M Tau was incubated at 37 $^{\circ}$ C with and without 40% (of Tau concentration) preformed A β 42 fibrils under quiescent conditions. e) The purity evaluation of NT-A β 42-CT was assessed by SDS-PAGE. f) Images of silk-like fiber generated from NT-A β 42-CT taken by confocal microscopy. The amplified areas are indicated by the dash boxes. The silk-like fiber was pulled from top to bottom direction. The scales bars are 50 μ m, 20 μ m, and 10 μ m, respectively, from left to right.

Taken together, both spidroin and pathogenic amyloidogenic peptide, capped with spidroin N- and C-terminal domains, can form macroscopic spider silk-like fibers, both of which consist of straight nanofibrils parallel to the fiber axis that is similar to native spider silk. It is not clear whether the amyloid-like nanofibrils are structurally identical to the nanofibrils constituting the silk-fibrils; however, the corresponding amyloid-like structures/properties of the amyloidogenic proteins/peptides might be preserved in the macroscopic fibers that could be a concern if these fibers are used in vivo. It has been shown that in transgenic mice, intravenous injection with preformed A β fibrils triggered IAPP amyloid formation in the pancreas of the mice, suggesting that A β could enhance IAPP amyloid formation through cross-seeding.^[76] Thus, silk-like fibers derived from pathogenic amyloid peptides (provided these peptides can form fibers) might preserve the cross-seeding capacity when implemented in vivo. The hybrid polypeptides with alternating amyloid and spider silk glycine-rich segments from *T. clavipes* MaSp1 assembled into β -sheet nanofibrils in buffer containing potassium phosphate with constant agitation.^[77] Intriguingly, these hybrid polymeric amyloid proteins were wet-spun into macroscopic fibers with excellent tensile strength.^[78] Modifying the amino acid sequences to increase the amyloidogenic propensity can improve the final mechanical properties of biomimetic spider silk fibers.^[79] However, modifications on original spidroin se-

quences might lead to different microscopic assemblies, and as it has been shown that silk nanofibrils from the cocoon of *B. mori* exert amyloid-accelerating properties in vivo,^[70] it might be important to consider the cross-seeding effects.

3. Conclusion

Spiders can produce various silk fibers with different functions, all of which are made from spidroins, and have strong amyloid-forming propensities. Interestingly, amyloid-like fibrils produced from spidroins are not significantly toxic when compared to amyloid fibrils derived from human pathogenic amyloidogenic peptides. The fundamental differences between the two types of nanofibrils are their primary structures and the mechanisms underlying their fibril formation. Spidroins use a non-nucleation-dependent isodesmic aggregation pathway, whereas pathogenic amyloidogenic peptides use a nucleation-dependent amyloid forming pathway. It is interesting that both types of proteins/peptides can assemble into solid macroscopic silk-like fibers consisting of nanofibrils; however, these two types of fibers might give different in vivo responses (cross-seeding effects). Future investigations of the inner structure of the nanofibrils in silk-like fibers and the in vivo toxic effects should be performed prior to implementation in vivo.

4. Experimental Section

Full-Length Spidroin Amyloid Prediction and Analysis: Amyloid nanofibrils exhibited a stacking columnar structure of β -strand-loop- β -strand motifs (also known as β -arch) with two β -strands interacting through their side chains rather than the backbone's hydrogen bonds as in conventional β -hairpins.^[80] When the β -arch was stacked into fibrillar structure β -arcade, its two strands were integrated into two different β -sheets.^[61] Using the structural insight of amyloid nanofibrils, the program ArchCandy was designed to estimate the probability of a given amino acid sequence to form β -arcade and predict the amyloidogenicity.^[45] The individual amyloidogenicity of the full-length MaSp1 and 2 (GeneBank accession number ABR68856 and ABR68855), MiSp (GeneBank accession number AFV31615), Flag (GeneBank accession number GIY90805), AcSp (GeneBank accession number AUH99620), TuSp (GeneBank accession number ASO67373), and PySp (GeneBank accession number GBN88500) was predicted by ArchCandy, where the scoring threshold was set to 0.575 as default. The structural arrangements of the spidroin amyloidogenic regions predicted by ArchCandy were further predicted by BetaSerpentine—predicts possible β -serpentine arrangements of adjacent β -arches.^[61] Default values were set for individual β -arches and β -serpentine thresholds (0.0 and 0.2, respectively). Amyloidogenic regions of the spidroins were also predicted by a consensus method AMYLPRED2 that employs a consensus of different methods specifically developed to predict features related to the formation of amyloid fibrils (<http://thalis.biol.uoa.gr/AMYLPRED2/>).^[81] The amino acid compositions of the full length spidroin amino acid sequences were analyzed by Geneious Prime.

Plasmid Construction and Recombinant Protein Preparation: A gene fragment encoding the 161-aa NT_{MiSp} followed by 261-aa repetitive sequence (referred to as NT-Rep_{MiSp}) of *A. ventricosus* MiSp was synthesized and inserted into pET-32a plasmid within NdeI and XhoI restriction sites. An enterokinase cleavage site (DDDDK) was introduced between the NT_{MiSp} and the repetitive sequence (Rep_{MiSp}). For plasmid pET-32a-NT_{MiSp}-Rep_{MiSp}-CT_{FISp} construction, the C-terminal gene sequence of *A. ventricosus* FISp (CT_{FISp}) was synthesized and fused to the C-terminal of NT-Rep_{MiSp} through XhoI restriction sites using the Seamless cloning strategy. Regarding the chimera protein NT_{MiSp}-A β ₄₂-CT_{FISp}, a fusion gene sequence including NT_{MiSp}, 42-aa human A β ₄₂ and CT_{FISp} was synthesized and inserted into pET-32a within NdeI and XhoI restriction sites to construct plasmid pET-32a-NT_{MiSp}-A β ₄₂-CT_{FISp}. All the constructs were confirmed by DNA sequencing, and the amino acids sequences were compiled in Table S2, Supporting Information.

The constructs were transformed into *E. coli* BL21 (DE3) competent cells individually. The cells were incubated at 37 °C in LB medium overnight and transferred into fresh LB medium with 100 μ g mL⁻¹ ampicillin. Protein expression was induced with 1 mM (final concentration) Isopropyl β -D-1-thiogalactopyranoside (IPTG) when OD₆₀₀ was 0.8–1.0 for 12 h at 25 °C. The cells were collected by centrifuge (5000 rpm, 20 min) and resuspended in 20 mM Tris pH 8.0. For protein purification, the cells were lysed by using High Pressure Homogenizer (PhD Technology LLC, USA) and centrifuged to obtain the inclusion bodies. Then the inclusion bodies were extensively washed and solubilized by a freeze-thawing strategy as previously described.^[82] The solubilized proteins were dialyzed in 10 mM Tris pH 8.0 to remove urea and the purity was assessed by SDS-PAGE. In order to generate protein Rep_{MiSp}, the NT_{MiSp}-Rep_{MiSp} proteins were cleaved by enterokinase and passed through Ni-NTA beads to remove the NT_{MiSp}. The fraction containing Rep_{MiSp} was further refined by a Superdex 75 26/600 column (cytiva) via an Äkta system to collect monomeric Rep_{MiSp} in 20 mM Tris pH 8.0. The recombinant A β ₄₂ peptide and tau protein were expressed and purified with using the NT* solubility tag as previously described,^[48] and the final monomeric species were refined by a Superdex 30 column and Superdex 200 column (cytiva) via an Äkta system, respectively.

Protein Stability Test, CD Measurement, and FTIR Analysis: Freshly prepared proteins Rep_{MiSp} in 10 mM Tris pH 8.0 with a final concentration of 250 μ g mL⁻¹ were incubated at 4 °C and room temperature, respectively. To test the protein stability 10 μ L protein samples from each group were collected at different incubation time intervals (until 7 days) for SDS-PAGE analysis. Regarding secondary structure evaluation, the recombi-

nant Rep_{MiSp} in 20 mM NaPi pH 8.0 was subjected to CD measurements. CD spectra were recorded in 1 mm path length quartz cuvettes at 25 °C from 260 to 185 nm using J-815 CD Spectrometer (JASCO, Japan), and the main parameters were as follows: wavelength step 0.5 nm, response time 1 s, and bandwidth 1 nm. The spectrum shown was the average from three continuous scans with background subtracted. For secondary structure evaluation analysis of the nanofibrils, the nanofibrils were placed onto a triple reflection horizontal ATR attachment. Absorption spectra were obtained by FTIR spectroscope (Bruker, Germany) with resolution of 2 cm⁻¹ within a wavenumber range of 400–4000 cm⁻¹ at room temperature. The second derivative was obtained from the amide I spectra region (range from 1595 to 1705 cm⁻¹) by using a third degree polynomial function. The background spectrum of a blank was subtracted. The nanofibrils was analyzed three times. The transmittance (T) was transformed into absorbance (A) according to the function $A = 2 - \log(\% T)$.^[59]

Thioflavin T Assay: For monitoring amyloid fibril formation and the kinetics, 20 μ L solution (20 mM Tris pH 8.0) containing monomeric Rep_{MiSp} at different concentrations (1.5, 2.0, 2.5, 3.0, 3.5, 4.0, and 4.8 μ mol L⁻¹) in the presence of 10 μ mol L⁻¹ ThT were added to each well of half-area 384-well black polystyrene microplates with clear bottom and nonbinding surface (Corning Glass 3766, USA), and incubated at 25 °C under quiescent conditions. The ThT fluorescence was continuously recorded using a 440 nm excitation filter and a 480 nm emission filter (FLUOStar Galaxy from BMG Labtech, Germany). For analysis of Rep_{MiSp} fibril formation kinetics in the presence of seeds, 20 μ L solution containing 4.8 μ mol L⁻¹ Rep_{MiSp} monomer, 10 μ mol L⁻¹ ThT, different concentrations (10%, 30%, and 50% of fresh Rep_{MiSp} molar concentration) of seeds (preformed Rep_{MiSp} fibrils, concentration was calculated from the original Rep_{MiSp} monomer concentration) were added at 4 °C to each well of half-area 96-well plates and incubated under quiescent conditions at 25 °C. The fluorescence was recorded as described above. Aggregation traces were normalized and averaged using four replicates for all the experiments. The fibrillar aggregation traces of Rep_{AcSp} (0.80 mg mL⁻¹ and 0.25 mg mL⁻¹) were monitored with similar settings as above but with shaking. For monitoring amyloid fibril formation of A β ₄₂, 20 μ L solution (20 mM NaPi pH 8.0 with 0.2 mmol L⁻¹ EDTA) containing monomeric A β ₄₂ at different concentrations (1.0, 1.5, 2.9, and 9 μ mol L⁻¹) in the presence of 10 μ mol L⁻¹ ThT were added to each well of half-area 384-well black polystyrene microplates with clear bottom and nonbinding surface (Corning Glass 3766, USA), and incubated at 37 °C under quiescent conditions. For the seeding experiment, 20 μ L solution containing 3 μ mol L⁻¹ A β ₄₂ monomer, 10 μ mol L⁻¹ ThT, and 0.6 nmol L⁻¹ preformed A β ₄₂ fibrils (seeds) were added at 4 °C to each well of half-area 96-well plates and incubated under quiescent conditions at 37 °C. For cross-seeding tau proteins, 20 μ L solution (20 mmol L⁻¹ NaPi pH 7.2 with 0.2 mmol L⁻¹ EDTA and 10 mmol L⁻¹ DTT) containing 3 μ mol L⁻¹ tau monomer, 10 μ mol L⁻¹ ThT, and 40% preformed A β ₄₂ fibrils (of fresh tau molar concentration) were added at 4 °C to each well of half-area 384-well plates and incubated under quiescent conditions at 37 °C.

Mass Photometry: Mass distribution of the filaments was measured using Refeyn 1 mass photometer. Filaments, formed at 4.6 μ mol L⁻¹ starting concentration at 37 °C for 65 h were used to measure the mass distribution. Tris buffer (9 μ L, 20 mmol L⁻¹ pH 8.0) was put on a glass for adjusting the focus of the instrument, then 9 μ L of filaments were added and 60 movie was recorded. The acquisition size was set to medium. Analysis of the movie was performed by built in software. The sample size was 4042 particles.

Kinetics Analysis: For the kinetic analysis BMG Fluorostra Omega plate reader was used. The filters were 450 nm for excitation and 480 nm for emission. Corning 384 black flat bottom plate was used, 50 μ L per well, 8 replicates. All starting solutions were kept on ice and 10 μ L of Thioflavin T was added to the protein aliquot. 20 mmol L⁻¹ Tris buffer pH 8 was used for aggregation. Filament molecular weight distribution (mass photometry) had a Poisson's shape, kinetic traces had no concentration dependence, and TEM images showed linear polymers. These observations strongly suggested chain polymerization mechanism, therefore modified version of the living polymerization model was used to fit the kinetic data as described in Equations (1) and (2).

Spider Silk-Like Fiber Generation and Observation by Confocal Microscopy: Spider silk-like fibers were manually drawn by hand from recombinant spider silk protein solution with a tip at room temperature. Briefly, 100 μL of recombinant protein (5 mg mL^{-1}) in 10 mmol L^{-1} Tris pH 8.0 was dropped onto a glass slide, and spider silk-like fibers were pulled from the solution with a continuous speed roughly. The hand-pulling silk-like fibers on the glass slide were observed with a Nikon A1 (Japan) confocal fluorescence microscope using their autofluorescence at 405 nm.

Transmission Electron Microscope: The morphology of the Rep_{MiSp} proteins at different time points were observed by transmission electron microscope (TEM). The Rep_{MiSp} samples after two days incubation were applied to carbon-coated copper grids (400 mesh, Analytical Standards) and incubated for 2 min. Excess solution was removed by blotting with filter paper (Whatman, grade 1) and the grids were washed with two drops of Milli-Q water. For staining, 7 μL of 2% uranyl acetate was added to each grid for 45 s before final blotting and air-drying. The grids were analyzed by transmission electron microscopy (TEM, Jeol JEM2100F at 200 kV). The diameter of the nanofibrils were analyzed by Fiji.^[46]

Preparation of Rep_{MiSp} Nanoparticles and Scanning Electron Microscopy: Rep_{MiSp} nanoparticles were prepared using a phase separation procedure as described previously.^[73] Briefly, 100 μL of Rep_{MiSp} (2.5 mg mL^{-1}) in 10 mmol L^{-1} Tris pH 8.0 were mixed with $1 \text{ mL } 2 \text{ mol L}^{-1}$ potassium phosphate at pH of 8.0 and incubated at room temperature for 2 h. The resulting particles were centrifuged for 20 min at $10\,000 \times g$ at 4°C and washed 3 times with MilliQ water. For scanning electron microscopy (SEM), the nanoparticles were air-dried on a silicon slice and sputtered with gold/palladium. Then nanoparticles were analyzed under a Hitachi S-4700 field emission scanning electron microscope (Hitachi, Japan) with 15 kV of accelerating voltage.

Cell Viability Test: The cytotoxicity test was performed on different cell lines, that is, HT29 and HeLa via CCK-8 Cell Proliferation Assay Kit (NCM biotech, China). Cells were plated in the 96-wells plates at a density of 30 000 cells per well and cultured in a humidified atmosphere containing 5% CO_2 at 37°C for 24 h, maintained in the media. Then, the soluble Rep_{MiSp}, Rep_{MiSp} nanofibrils or the Rep_{MiSp} nanoparticles were added to the 96-wells plates, respectively, to yield final concentrations of 50 100, and $250 \mu\text{g mL}^{-1}$. After 24 h of incubation, the CCK8 assay was performed. Briefly, 10 μL CCK-8 solution was added to each well and incubated for 4 h at room temperature. The viability of cells was measured by detecting absorbance at 450 nm using a microplate reader (Thermo Scientific, USA). The experiments were repeated three times.

Statistical Analysis: Statistically analyses were performed in Prism 9. The multiple groups were statistically compared with the ordinary one-way analysis of variance (ANOVA) following by multiple comparisons with Tukey correction. Significance levels are $*p < 0.05$; $**p < 0.01$; $***p < 0.001$; $****p < 0.0001$. ns, no significant difference. Data are presented as mean \pm SD.

Supporting Information

Supporting Information is available from the Wiley Online Library or from the author.

Acknowledgements

X.Q. and Y.W. contributed equally to this work. This study was supported by the National Nature Science Foundation of China (No. 31771003) and the Priority Academic Program Development of Jiangsu Higher Education Institutions (PAPD). G.C. is supported by the Alzheimer's Association Research Grant, Olle Engkvists Stiftelse, the Petrus and Augusta Hedlunds Stiftelse, Åke Wibergs stiftelse, the Swedish Alzheimer foundation, the Åhlén Stiftelsens, Karolinska Institutet Research Foundation Grant, the Stiftelsen för Gamla Tjänarinnor, the Stiftelsen Sigurd och Elsa Goljes Minne, the Loo and Hans Osterman Foundation, Geriatric Diseases Foundation at Karolinska Institutet, the Gun and Bertil Stohne's Foundation and the Magnus Bergvall foundation. X.Z., Z.J., and Z.Z. are supported by the

China Scholarship Council. Y.W. is supported by the China Association for Science and Technology. [Correction added on November 15th, 2023 after first online publication: PAPD was acknowledged as a funding source.]

Conflict of Interest

The authors declare no conflict of interest.

Data Availability Statement

The data that support the findings of this study are available on request from the corresponding author. The data are not publicly available due to privacy or ethical restrictions.

Keywords

cytotoxicity, nanofibril, non-nucleation-dependent polymerization, seeding, spidroin

Received: May 13, 2023
Revised: June 29, 2023
Published online: July 16, 2023

- [1] C. P. J. Maury, *Cell Mol. Life Sci.* **2018**, *75*, 1499.
- [2] M. D. Benson, J. N. Buxbaum, D. S. Eisenberg, G. Merlini, M. J. M. Saraiva, Y. Sekijima, J. D. Sipe, P. Westermark, *Amyloid* **2018**, *25*, 215.
- [3] M. Landreh, M. R. Sawaya, M. S. Hipp, D. S. Eisenberg, K. Wuthrich, F. U. Hartl, *J. Int. Med.* **2016**, *280*, 164.
- [4] P. Falabella, L. Riviello, M. Pascale, I. D. Lelio, G. Tettamanti, A. Grimaldi, C. Iannone, M. Monti, P. Pucci, A. M. Tamburro, M. Deeguileor, S. Gigliotti, F. Pennacchio, *Insect Biochem. Mol. Biol.* **2012**, *42*, 203.
- [5] J. M. Kenney, D. Knight, M. J. Wise, F. Vollrath, *Eur. J. Biochem.* **2002**, *269*, 4159.
- [6] D. Romero, C. Aguilar, R. Losick, R. Kolter, *Proc. Natl. Acad. Sci. U. S. A.* **2010**, *107*, 2230.
- [7] F. Chiti, C. M. Dobson, *Annu. Rev. Biochem.* **2017**, *86*, 27.
- [8] M. Varadi, G. De Baets, W. F. Vranken, P. Tompa, R. Pancsa, *Nucleic Acids Res.* **2018**, *46*, D387.
- [9] C. Frieden, *Protein Sci.* **2007**, *16*, 2334.
- [10] S. I. Cohen, S. Linse, L. M. Luheshi, E. Hellstrand, D. A. White, L. Rajah, D. E. Otzen, M. Vendruscolo, C. M. Dobson, T. P. Knowles, *Proc. Natl. Acad. Sci. U. S. A.* **2013**, *110*, 9758.
- [11] D. C. Rodriguez Camargo, S. Chia, J. Menzies, B. Mannini, G. Meisl, M. Lundqvist, C. Pohl, K. Bernfur, V. Lattanzi, J. Habchi, S. I. Cohen, T. P. J. Knowles, M. Vendruscolo, S. Linse, *Front. Mol. Biosci.* **2021**, *8*, 1037.
- [12] M. Sleutel, I. Van den Broeck, N. Van Gerven, C. Feuille, W. Jonckheere, C. Valotteau, Y. F. Dufrêne, H. Remaut, *Nat. Chem. Biol.* **2017**, *13*, 902.
- [13] A. J. Geddes, K. D. Parker, E. D. Atkins, E. Beighton, *J. Mol. Biol.* **1968**, *32*, 343.
- [14] A. Rising, J. Johansson, *Nat. Chem. Biol.* **2015**, *11*, 309.
- [15] A. P. Kiseleva, P. V. Krivoschapkin, E. F. Krivoschapkina, *Front. Chem.* **2020**, *8*, 554.
- [16] Q. Wang, H. C. Schniepp, *JOM* **2019**, *71*, 1248.
- [17] J. H. He, Y. Liu, L. Xu, J. Y. Yu, G. Sun, *Chaos, Solitons Fractals* **2008**, *37*, 643.
- [18] D. P. Knight, F. Vollrath, *Biol. Sci.* **2002**, *357*, 219.

- [19] Z. Yang, D. T. Grubb, L. W. Jelinski, *Macromolecules* **1997**, *30*, 8254.
- [20] M. Kitagawa, T. Kitayama, *J. Mater. Sci.* **1997**, *32*, 2005.
- [21] N. Du, X. Y. Liu, J. Narayanan, L. Li, M. L. Lim, D. Li, *Biophys. J.* **2006**, *91*, 4528.
- [22] L. P. Silva, E. L. Rech, *Nat. Commun.* **2013**, *4*, 3014.
- [23] A. Sponner, W. Vater, S. Monajembashi, E. Unger, F. Grosse, K. Weissart, *PLoS One* **2007**, *2*, e998.
- [24] K. Augsten, P. Muhlig, C. Herrmann, *Scanning* **2000**, *22*, 12.
- [25] P. Poza, J. Pérez-Rigueiro, M. Elices, J. Llorca, *Eng Fract. Mech.* **2002**, *69*, 1035.
- [26] C. Riekel, M. Burghammer, T. G. Dane, C. Ferrero, M. Rosenthal, *Biomacromolecules* **2017**, *18*, 231.
- [27] I. Iachina, J. Fiutowski, H. G. Rubahn, F. Vollrath, J. R. Brewer, *Sci. Rep.* **2023**, *13*, 6695.
- [28] O. Hakimi, D. P. Knight, M. M. Knight, M. F. Grahn, P. Vadgama, *Biomacromolecules* **2006**, *7*, 2901.
- [29] C. F. Hu, Z. G. Qian, Q. Peng, Y. Zhang, X. X. Xia, *ACS Biomater. Sci. Eng.* **2021**, *7*, 3608.
- [30] M. L. Tremblay, L. Xu, T. Lefevre, M. Sarker, K. E. Orrell, J. Leclerc, Q. Meng, M. Pezolet, M. Auger, X. Q. Liu, J. K. Rainey, *Sci. Rep.* **2015**, *5*, 11502.
- [31] S. Rammensee, D. Huemmerich, K. D. Hermanson, T. Scheibel, A. R. Bausch, *Appl. Phys. A* **2006**, *82*, 261.
- [32] U. Slotta, S. Hess, K. Spiess, T. Stromer, L. Serpell, T. Scheibel, *Macromol. Biosci.* **2007**, *7*, 183.
- [33] M. Humenik, M. Magdeburg, T. Scheibel, *J. Struct. Biol.* **2014**, *186*, 431.
- [34] K. Numata, D. L. Kaplan, *Macromol. Biosci.* **2011**, *11*, 60.
- [35] M. Andersson, G. Chen, M. Otikovs, M. Landreh, K. Nordling, N. Kronqvist, P. Westermark, H. Jornvall, S. Knight, Y. Ridderstrale, L. Holm, Q. Meng, K. Jaudzems, M. Chesler, J. Johansson, A. Rising, *PLoS Biol.* **2014**, *12*, e1001921.
- [36] X. Li, J. S. Fan, M. Shi, C. C. Lai, J. Li, Q. Meng, D. Yang, *Biomacromolecules* **2022**, *23*, 1643.
- [37] T. Arndt, K. Jaudzems, O. Shilkova, J. Francis, M. Johansson, P. R. Laity, C. Sahin, U. Chatterjee, N. Kronqvist, E. Barajas-Ledesma, R. Kumar, G. Chen, R. Stromberg, A. Abelein, M. Langton, M. Landreh, A. Barth, C. Holland, J. Johansson, A. Rising, *Nat. Commun.* **2022**, *13*, 4695.
- [38] T. Lefevre, S. Boudreault, C. Cloutier, M. Pezolet, *J. Mol. Biol.* **2011**, *405*, 238.
- [39] I. A. Iashchishyn, D. Sulskis, M. Nguyen Ngoc, V. Smirnovas, L. A. Morozova-Roche, *ACS Chem. Neurosci.* **2017**, *8*, 2152.
- [40] M. Mališauskas, V. Zamotin, J. Jass, W. Noppe, C. M. Dobson, L. A. Morozova-Roche, *J. Mol. Biol.* **2003**, *330*, 879.
- [41] H. J. Jin, D. L. Kaplan, *Nature* **2003**, *424*, 1057.
- [42] F. Vollrath, D. P. Knight, *Nature* **2001**, *410*, 541.
- [43] A. D. Malay, T. Suzuki, T. Katashima, N. Kono, K. Arakawa, K. Numata, *Sci Adv* **2020**, *6*, eabb6030.
- [44] G. Chen, X. Liu, Y. Zhang, S. Lin, Z. Yang, J. Johansson, A. Rising, Q. Meng, *PLoS One* **2012**, *7*, e52293.
- [45] A. B. Ahmed, N. Znassi, M. T. Chateau, A. V. Kajava, *Alzheimers Dementia* **2015**, *11*, 681.
- [46] J. Schindelin, I. Arganda-Carreras, E. Frise, V. Kaynig, M. Longair, T. Pietzsch, S. Preibisch, C. Rueden, S. Saalfeld, B. Schmid, J. Y. Tinevez, D. J. White, V. Hartenstein, K. Eliceiri, P. Tomancak, A. Cardona, *Nat. Methods* **2012**, *9*, 676.
- [47] A. Avni, H. M. Swasthi, A. Majumdar, S. Mukhopadhyay, *Prog. Mol. Biol. Transl. Sci.* **2019**, *166*, 109.
- [48] X. Zhong, R. Kumar, Y. Wang, H. Biverstal, C. I. Jegerschold, P. J. B. Koock, J. Johansson, A. Abelein, G. Chen, *ACS Chem. Biol.* **2022**, *17*, 2201.
- [49] D. Perera, L. Li, C. Walsh, Q. Wang, H. C. Schniepp, *arXiv* **2022**, 2207, 06535.
- [50] P. L. Babb, N. F. Lahens, S. M. Correa-Garhwal, D. N. Nicholson, E. J. Kim, J. B. Hogenesch, M. Kuntner, L. Higgins, C. Y. Hayashi, I. Agnarsson, B. F. Voight, *Nat. Genet.* **2017**, *49*, 895.
- [51] N. A. Ayoub, J. E. Garb, R. M. Tinghitella, M. A. Collin, C. Y. Hayashi, *PLoS One* **2007**, *2*, e514.
- [52] C. Y. Hayashi, R. V. Lewis, *Bioessays* **2001**, *23*, 750.
- [53] C. Y. Hayashi, R. V. Lewis, *Science* **2000**, *287*, 1477.
- [54] K. Wang, R. Wen, Q. Jia, X. Liu, J. Xiao, Q. Meng, *Genes (Basel)* **2019**, *10*, 425.
- [55] R. Wen, K. Wang, Q. Meng, *Int. J. Biol. Macromol.* **2020**, *160*, 806.
- [56] R. Wen, K. Wang, Q. Meng, *Int. J. Biol. Macromol.* **2020**, *157*, 60.
- [57] L. Xu, J. K. Rainey, Q. Meng, X. Q. Liu, *PLoS One* **2012**, *7*, e50227.
- [58] C. Y. Hayashi, N. H. Shipley, R. V. Lewis, *Int. J. Biol. Macromol.* **1999**, *24*, 271.
- [59] X. Li, X. Qi, Y. M. Cai, Y. Sun, R. Wen, R. Zhang, J. Johansson, Q. Meng, G. Chen, *ACS Biomater. Sci. Eng.* **2022**, *8*, 119.
- [60] Q. Jia, R. Wen, Q. Meng, *Int. J. Mol. Sci.* **2020**, *21*, 6905.
- [61] S. A. Bondarev, O. V. Bondareva, G. A. Zhouravleva, A. V. Kajava, *Bioinformatics* **2018**, *34*, 599.
- [62] Q. Wang, P. McArdle, S. L. Wang, R. L. Wilmington, Z. Xing, A. Greenwood, M. L. Cotten, M. M. Qazilbash, H. C. Schniepp, *Nat. Commun.* **2022**, *13*, 4329.
- [63] G. Meisl, X. Yang, E. Hellstrand, B. Frohm, J. B. Kirkegaard, S. I. Cohen, C. M. Dobson, S. Linse, T. P. Knowles, *Proc. Natl. Acad. Sci. U. S. A.* **2014**, *111*, 9384.
- [64] G. R. Strobl, *The Physics of Polymers: Concepts for Understanding Their Structures and Behavior*, 2nd ed., Springer, Berlin **1997**, p. 450.
- [65] X. Chen, Z. Shao, D. P. Knight, F. Vollrath, *Proteins* **2007**, *68*, 223.
- [66] A. R. Hurshman, J. T. White, E. T. Powers, J. W. Kelly, *Biochemistry* **2004**, *43*, 7365.
- [67] A. Leppert, G. Chen, D. Lama, C. Sahin, V. Railaite, O. Shilkova, T. Arndt, E. G. Marklund, D. P. Lane, A. Rising, M. Landreh, *Nano Lett.* **2023**, *23*, 5836.
- [68] M. Humenik, A. M. Smith, S. Arndt, T. Scheibel, *J. Struct. Biol.* **2015**, *191*, 130.
- [69] S. Subedi, S. Sasidharan, N. Nag, P. Saudagar, T. Tripathi, *Molecules* **2022**, *27*, 1776.
- [70] K. Lundmark, G. T. Westermark, A. Olsén, P. Westermark, *Proc. Natl. Acad. Sci. U. S. A.* **2005**, *102*, 6098.
- [71] A. Rising, P. Gherardi, G. Chen, J. Johansson, M. E. Oskarsson, G. T. Westermark, P. Westermark, *Sci. Rep.* **2021**, *11*, 21069.
- [72] K. Numata, P. Cebe, D. L. Kaplan, *Biomaterials* **2010**, *31*, 2926.
- [73] H. Cai, G. Chen, H. Yu, Y. Tang, S. Xiong, X. Qi, *BMC Biotechnol.* **2020**, *20*, 37.
- [74] D. J. Selkoe, J. Hardy, *EMBO Mol. Med.* **2016**, *8*, 595.
- [75] L. Eisoldt, C. Thamm, T. Scheibel, *Biopolymers* **2012**, *97*, 355.
- [76] M. E. Oskarsson, J. F. Paulsson, S. W. Schultz, M. Ingelsson, P. Westermark, G. T. Westermark, *Am. J. Pathol.* **2015**, *185*, 834.
- [77] B. Dai, C. J. Sargent, X. Gui, C. Liu, F. Zhang, *Biomacromolecules* **2019**, *20*, 2015.
- [78] J. Li, Y. Zhu, H. Yu, B. Dai, Y. S. Jun, F. Zhang, *ACS Nano* **2021**, *15*, 11843.
- [79] T. Arndt, G. Greco, B. Schmuck, J. Bunz, O. Shilkova, J. Francis, N. M. Pugno, K. Jaudzems, A. Barth, J. Johansson, A. Rising, *Adv. Funct. Mater.* **2022**, *32*, 2200986.
- [80] M. R. Sawaya, M. P. Hughes, J. A. Rodriguez, R. Riek, D. S. Eisenberg, *Cell* **2021**, *184*, 4857.
- [81] A. C. Tsois, N. C. Papandreou, V. A. Iconomidou, S. J. Hamodrakas, *PLoS One* **2013**, *8*, e54175.
- [82] X. Qi, Y. Sun, S. Xiong, *Microb. Cell Fact.* **2015**, *14*, 24.